Heat and mass transfer during a sudden loss of vacuum in a liquid helium cooled tube - Part III: Heat deposition in He II

Nathaniel Garceau [a,b], Shiran Bao [a,b], Wei Guo [a,b,*]

[a] *National High Magnetic Field Laboratory, 1800 East Paul Dirac Drive. Tallahassee, FL 32310, USA*
[b] *Mechanical Engineering Department, FAMU-FSU College of Engineering, Florida State University, Tallahassee, FL 32310, USA*

ABSTRACT

A sudden loss of vacuum can be catastrophic for superconducting particle accelerators. In such an event, air leaks into the liquid-helium-cooled accelerator beamline tube and condenses on its inner surface, causing rapid boiling of the helium and dangerous pressure build-up. Understanding the coupled heat and mass transfer processes is important for the design of the beamline cryogenic system. Our past experimental study on nitrogen gas propagating in a copper tube cooled by normal liquid helium (He I) has revealed a nearly exponential slowing down of the gas front. A theoretical model that accounts for the interplay of the gas dynamics and the condensation was developed, which successfully reproduced various key observations. However, since many accelerator beamlines are actually cooled by superfluid helium (He II) in which the heat transfer is via a non-classical thermal counterflow mode, we need to extend our work to the He II cooled tube. This paper reports our systematic measurements using He II and the numerical simulations based on a modified model that accounts for the He II heat-transfer characteristics. By tuning the He II peak heat-flux parameter in our model, we have reproduced the observed gas dynamics in all experimental runs. The fine-tuned model is then utilized to reliably evaluate the heat deposition in He II. This work not only advances our understanding of condensing gas dynamics but also has practical implications to the design codes for beamline safety.

1. Introduction

Many modern particle accelerators utilize superconducting radio-frequency (SRF) cavities cooled by liquid helium (LHe) to accelerate particles [1]. These SRF cavities are housed inside interconnected cryomodules and form a long LHe-cooled vacuum tube, i.e., the beamline tube [2]. An accelerator can experience a catastrophic breakdown if the cavities accidentally lose their vacuum to the surrounding atmosphere. For example, an accidental rupture at a cryomodule interconnect will provide the room-temperature air an open path to enter the cavity space. The air can then condense on the cavity's inner surface and rapidly deposit heat to the LHe, causing violent boiling in LHe and dangerous pressure build-up in the cryomodule. Safety concerns and possible damage as a result of a sudden vacuum loss have led to multiple failure studies at accelerator labs [3–8]. These preliminary studies revealed that the gas propagation in a freezing vacuum tube can slow down substantially as compared to that in a room-temperature tube.

In order to better understand the complex coupled heat and mass transfer processes involved in a beamline vacuum break event, pioneering work has been carried out in our cryogenics lab by Dhuley and Van Sciver via venting room-temperature nitrogen (N_2) gas from a buffer tank to a LHe cooled vacuum tube [9,10]. Their experiments with normal liquid helium (He I) showed that the gas-front propagation slowed down nearly exponentially. This deceleration was attributed to gas condensation to the tube wall [10], but a quantitative analysis on how the condensation leads to the observed exponential slowing down was not provided. Another limitation in these early experiments is that the tube system was not suitable for measurements with the superfluid phase of liquid helium (He II). This is because after the helium bath is pumped to the He II phase, only a small section of the tube can remain immersed in He II. Furthermore, the tube section above the liquid level can be effectively cooled by the flowing helium vapor to sufficiently low temperatures such that the nitrogen gas may condense at an unknown location in this tube section. This uncertainty makes subsequent data analysis and result interpretation difficult.

In our later systematic work, a longer helical tube system was fabricated [11]. The tube section above the liquid surface is pro-

* Corresponding author at: Mechanical Engineering Department, FAMU-FSU College of Engineering, Florida State University, Tallahassee, FL 32310, USA.
  E-mail address: wguo@magnet.fsu.edu (W. Guo).

Nomenclature

A_{GM}	Gorter-Mellink mutual friction parameter
C	Specific heat (J/(kg·K))
D_1	Inner diameter of the tube (m)
D_2	Outer diameter of the tube (m)
$f(T)$	He II heat conductivity function (W/(m^5·K))
g	Gravitational acceleration (m/s^2)
h	He II depth (m)
$\hat{h}$	Specific enthalpy (J/kg)
h_{film}	Film boiling coefficient (W/(m^2·K))
k	Thermal conductivity (W/(m·K))
L	Tube length (m)
$\dot{m}_c$	Mass deposition flux (kg/(m^2·s))
M_g	Gas molar mass (kg/mol)
n	Kapitza conduction parameter
Nu	Nusselt number
P	Pressure (Pa)
P_h	Hydrostatic head pressure (Pa)
q_{dep}	Deposition heat flux (W/m^2)
q_{He}	Heat flux to He II bath (W/m^2)
q_i	Heat flux to tube inner surface (W/m^2)
q_0^*	Peak heat flux (W/m^2)
Q	Total heat deposited in He II (kJ)
R	Ideal gas constant (J/(mol·K))
s	Specific entropy (J/(kg·K))
t	Time (s)
t_r	Rise time (s)
T	Temperature (K)
T_{sat}	Saturation temperature (K)
v	Gas velocity along pipe (m/s)
u	Radial mean velocity (m/s)
u_T	Gas molecule thermal velocity (m/s)
x	Coordinate along the tube (m)

Greeks

α	Kapitza conductance parameter (kW/(m^2·K^n))
β	Ratio of velocity, u/u_T
Γ	Velocity distribution correction factor
δ	Thickness of the solid nitrogen layer (m)
ΔT	Temperature difference, $T_w - T_{bath}$ (K)
ε	Specific internal energy (J/kg)
μ	Viscosity (Pa·s)
ρ	Density (kg/m^3)
ρ_{He}	He II density (kg/m^3)
ρ_n	Normal fluid density (kg/m^3)
ρ_s	Super fluid density (kg/m^3)
σ_c	Condensation coefficient
σ_e	Evaporation coefficient
ψ	Empirical parameter in the peak heat flux model

Subscripts

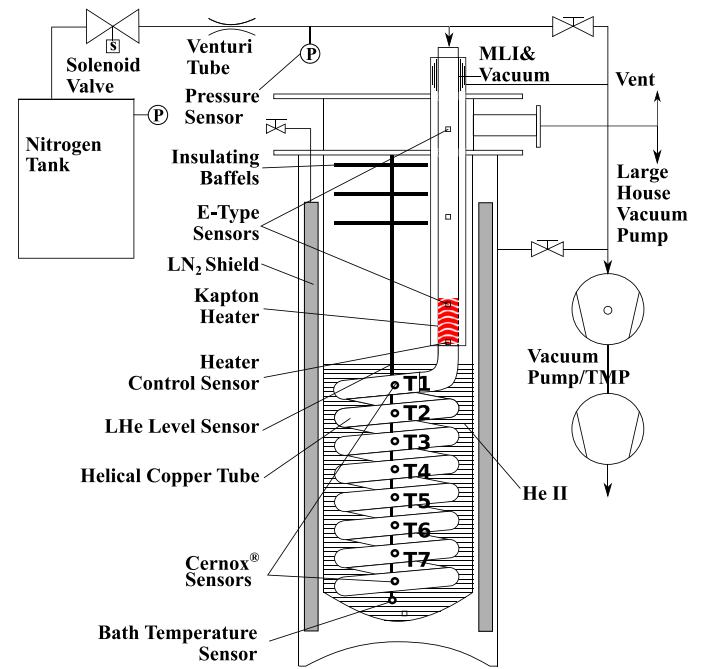|	
$bath$	Helium bath
c	Center of the frost layer
g	Bulk gas
s	Surface of the frost layer
SN	Solid nitrogen
w	Copper tube wall
λ	Lambda point

Fig. 1. Schematic diagram of the experimental setup used in our study on vacuum break in the He II cooled tube.

tions. Our systematic measurements with He I confirmed the observed slowing down of the gas-front propagation [13]. A theoretical model that accounts for the gas dynamics, surface condensation, and heat transfer to He I was also developed, which successfully reproduced various key observations [14]. On the other hand, since many accelerator beamlines are actually cooled by He II whose heat transfer characteristics are controlled by a nonclassical thermal counterflow mode [15], the insights gained in our He I studies are not all directly applicable. For this reason, we now extend our work to the He II cooled tube.

This paper reports our systematic experimental measurements with He II as well as our numerical simulations of the relevant heat and mass transfer processes. In Section 2, we discuss our experimental setup, the measurement procedures, and the main observations. In Section 3, we present our theoretical model which consists of the conservation equations of the propagating gas, a refined model of the gas condensation, and a correlation model that reasonably describes the heat transfer in He II. The validation of the model is discussed in Section 4. We show that by tuning the He II peak heat-flux parameter in our model, the observed gas motion under various inlet gas pressures and mass flow rates can be well reproduced. In Section 5, we present the calculated heat-deposition rate in He II using the fine-tuned model. Finally, a brief summary is included in Section 6. Our systematic work provides an unprecedented characterization of the heat load accompanying the vacuum break in a He II cooled tube, which could have important implications to the design and safe operation of beamline cryogenic systems.

2. Experimental measurements

The apparatus used in our He II experiment is the same as that in our prior He I experiment. The details of the setup can be found in [13,14,16]. In summary, the system includes a copper tube with a total length of 5.75 m. The tube has an outer diameter of 2.8 cm and a wall thickness of 1.25 mm. It is bent into a helical coil shape with a coil diameter of 22.9 cm, as shown in Fig. 1. The copper tube is soldered to a stainless steel extension tube which connects

tected by a vacuum jacket and its temperature is always maintained to above 77 K using a feedback-controlled heater system [12]. This design allows us to accurately control the starting location of the gas condensation, which is crucial for reliable measurements and for convenient comparison with model simula-
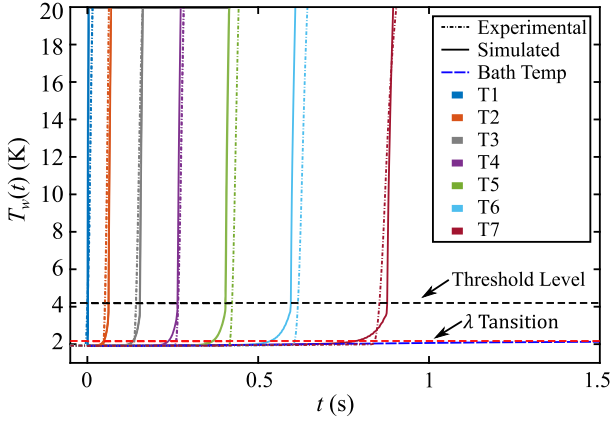
Fig. 2. Measured and simulated wall temperature curves at different sensor locations for the experimental run at 150 kPa tank pressure.

Fig. 3. Measured and simulated rise times of the temperature curves at different sensor locations for experimental runs with different tank pressures.

to the outside plumbing. The extension tube is vacuum insulated to prevent variations in temperature that could be resulted from convective cooling due to the flowing vapor during the bath pumping [12]. The liquid level in the bath is controlled such that upon the completion of the pumping to a desired He II temperature, the helical copper tube is completely immersed in He II.

2.1. Experimental procedures

In our experiments, pure nitrogen gas contained in a 230-L reservoir tank was used to maintain consistent flow conditions. Vacuum break was simulated by opening a fast-action solenoid valve (25 ms opening time). Following the solenoid valve, a venturi tube choked the gas flow into the evacuated tube system such that the gas velocity at the venturi exit reached the local sound speed. The gas pressures in the nitrogen tank and after the venturi were monitored using Kulite® XCQ-092 high speed pressure sensors. Data acquisition was conducted at a rate of 4800 Hz using LabVIEW® and four data acquisition modules (i.e., DT9824 from Data Translation Inc.). Measurements at four different tank pressures, i.e., 50 kPa, 100 kPa, 150 kPa, and 200 kPa, were conducted.

The gas propagation was measured by monitoring the surface temperature of the copper tube using seven Lake Shore Cernox® temperature sensors encapsulated in 2850 FT Stycast® epoxy [17]. These sensors were mounted on the outer surface of the copper tube using hose clamps and were placed at 72 cm apart along the tube. To reduce the thermal contact resistance between the sensors and the copper tube, indium foil and Apliezon® N thermal grease were applied at the interface. To monitor the bath temperature, one Cernox sensor was allowed to float in the center of the helium bath, as shown in Fig. 1.

2.2. Main observations

After the solenoid valve was opened, the nitrogen gas flushed into the evacuated copper tube and condensed on the tube inner surface, causing variations of the tube-wall temperature $T_w(x, t)$. Fig. 2 shows the wall temperature curves recorded by the Cernox sensors in a representative experimental run with a tank pressure of 150 kPa. These curves initially remain at the bath temperature (i.e., 1.95 K). Upon the arrival of the propagating gas font, the temperature curves rise sharply to a saturation level of about 50 K to 60 K (not shown in the figure). Due to the heat deposited in the bath, the bath temperature T_{bath} also rises steadily. Nevertheless, according to the T_{bath} curve, the LHe remained in the He II phase since its temperature was below the lambda-point temperature (i.e., $T_\lambda = 2.17$ K) over the course of the experiment. There-
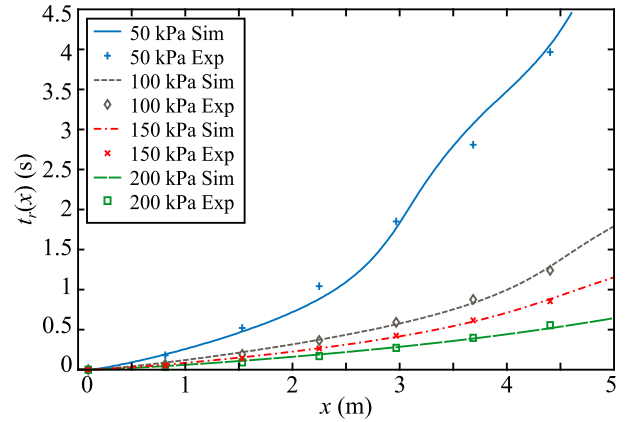
fore, the He II heat transfer characteristics are relevant in our result analysis.

In order to extract quantitative information about the gas propagation, we introduce a rise time $t_r(x)$ defined as the moment when the temperature at a distance x along the tube from the coil entrance rises to above a threshold level of 4.2 K, as indicated in Fig. 2. This threshold level is chosen arbitrarily. However, our tests indicate that the threshold level does not affect too much our later model fitting results as long as the threshold level is chosen in the sharp-rising region of the temperature curves. The rise times recorded at different sensor locations for all the four runs with tank pressures of 50 kPa, 100 kPa, 150 kPa, and 200 kPa are collected in Fig. 3. At 50 kPa tank pressure and hence the lowest tube inlet mass flow rate, the slowest propagation and the strongest deceleration of the gas flow were observed. On the other hand, at 200 kPa tank pressure, the mean velocity of the gas is the highest (i.e., about 10 m/s) and the slowing-down effect is relatively mild.

3. Theoretical model

We describe the N_2 gas dynamics and the heat transfer in our He II cooled tube using an one-dimensional (1D) model similar to that discussed in our previous work [14]. This 1D modeling is reasonable considering the small diameter-to-length ratio of the tube. A refined gas condensation model and a heat-transfer correlation model applicable to He II are incorporated in the current work. In what follows, we outline the relevant details.

3.1. Gas dynamics

The propagation of the N_2 gas in the tube and the evolution of its properties can be described by the conservation equations of the N_2 mass, momentum, and energy, as listed below:

$$\frac{\partial \rho_g}{\partial t} + \frac{\partial}{\partial x}(\rho_g v) = -\frac{4}{D_1}\dot{m}_c, \tag{1}$$

$$\frac{\partial}{\partial t}(\rho_g v) + \frac{\partial}{\partial x}(\rho_g v^2) = -\frac{\partial P}{\partial x} - \frac{4}{D_1}\dot{m}_c v, \tag{2}$$

$$\frac{\partial}{\partial t}\left[\rho_g\left(\varepsilon_g + \frac{1}{2}v^2\right)\right] + \frac{\partial}{\partial x}\left[\rho_g v\left(\varepsilon_g + \frac{1}{2}v^2 + \frac{P}{\rho_g}\right)\right]$$

$$= -\frac{4}{D_1}\dot{m}_c\left(\varepsilon_g + \frac{1}{2}v^2 + \frac{P}{\rho_g}\right) - \frac{4}{D_1^2}Nu \cdot k_g(T_g - T_s). \tag{3}$$

The definitions of the parameters involved in the above equations are provided in the Nomenclature table. These equations, including

the Nusselt number Nu correlation for gas convective heat transfer, are the same as in our prior modeling work [14], which are also similar to those reported in Ref. [18,19]. The model assumes the ideal-gas equation of state for the N_2 gas:

$$PM_g = \rho_g RT_g, \tag{4}$$

which is justified since the compressibility of the N_2 gas is close to unity in the entire experiment [14]. The terms containing $\dot{m}_c$ on the right hand side of the Eq. (1)–(3) account for the effects due to the condensation of the N_2 gas on the tube inner surface. The parameter $\dot{m}_c$ denotes the mass deposition rate per unit tube inner surface area, which requires an additional equation to describe its time evolution.

3.2. Mass deposition

In our previous work [14], $\dot{m}_c$ is evaluated using a sticking co-efficient model derived assuming an ideal Maxwellian velocity distribution of the gas molecules. Although this model is designed for use in the free molecular flow regime, it turns out to describe well the mass deposition in our He I experiments where the N_2 gas was essentially in the continuum flow regime [13]. Nevertheless, potential inaccuracy may still occur when $\dot{m}_c$ is so large that the distribution of the molecule velocity starts to deviate from the Maxwellian distribution due to the mean flow towards the wall as caused by condensation.

To account for this effect, in the current work we adopt a refined model using the Hertz-Knudsen relation with the Schrage modification [20]. This kinetic theory model evaluates $\dot{m}_c$ based on the difference between the flux of the molecules condensing on the cold surface and the flux of the molecules getting evaporated from the frost layer:

$$\dot{m}_c = \sqrt{\frac{M_g}{2\pi R}}\left(\Gamma \sigma_c \frac{P}{\sqrt{T_g}} - \sigma_e \frac{P_s}{\sqrt{T_s}}\right), \tag{5}$$

where P_s is the saturated vapor pressure at the frost-layer surface temperature T_s. σ_c and σ_e are empirical condensation and evaporation coefficients which are typically about the same and close to unity for a very cold surface [21]. We take 0.95 for both coefficients in our later numerical simulations. The coefficient Γ is responsible for any deviation from the Maxwellian velocity distribution of the molecules as caused by the condensation on the wall. In terms of the mean-flow velocity towards the cold wall $u = \dot{m}_c/\rho_g$, Γ can be calculated as [20]:

$$\Gamma(\beta) = exp(-\beta^2) + \beta\sqrt{\pi}[1 + erf(\beta)], \tag{6}$$

where $\beta = u/u_T$ with $u_T = \sqrt{2RT_g/M_g}$ being the thermal velocity of the gas molecules. Note that since Γ depends on $\dot{m}_c$ through u, the Eq. (5) needs to be solved self-consistently at every time step to obtain the evolution of $\dot{m}_c$.

3.3. Radial heat transfer

In the governing equations for the gas dynamics and $\dot{m}_c$, the surface temperature T_s of the frost layer is needed. This information can be obtained through the analysis of the heat transfer in the radial direction.

First, assuming that the frost-layer thickness δ is small such that a linear temperature profile exists in the layer, we can evaluate the frost-layer center temperature $T_c = (T_w + T_s)/2$ as [14]:

$$\rho_{SN}C_{SN}\delta\frac{\partial T_c}{\partial t} = q_{dep} - q_i \tag{7}$$

where $q_{dep} = \dot{m}_c[v^2/2 + \hat{h}_g - \hat{h}_s] + Nu \cdot k_g(T_g - T_s)/D_1$ is the total incoming heat flux to the frost layer, and $q_i = k_{SN}(T_s - T_w)/\delta$ denotes the outgoing heat flux to the copper tube wall. The growth rate of the frost layer thickness δ is given by $\delta = \dot{m}_c/\rho_{SN}$.

Then, the variation of the copper tube wall temperature T_w can be described by:

$$\rho_w C_w \frac{D_2^2 - D_1^2}{4D_1}\frac{\partial T_w}{\partial t} = q_i - q_{He}\frac{D_2}{D_1} + \frac{D_2^2 - D_1^2}{4D_1}k_w\frac{\partial^2 T_w}{\partial x^2}. \tag{8}$$

In this equation, we neglected the temperature gradient across the thickness of the copper tube, which is justified considering the high thermal conductivity of copper and the small wall thickness. The parameter q_{He} denotes the heat flux from the copper tube to the He II bath, which is modeled separately.

3.4. He II heat transfer modeling

It has been known that He II can be treated as a mixture of two miscible fluid components: an inviscid and zero-entropy su-perfluid and a viscous normal fluid [22]. Heat transfer in bulk He II is via an extremely effective counterflow mode instead of classical convection [15]: the normal fluid carries the heat away from the heat source at a velocity proportional to the heat flux, whereas the superfluid moves in the opposite direction to en-sure mass conservation. When the heat flux exceeds a small crit-ical value, quantized vortices are nucleated spontaneously in the superfluid, which can impede the counterflow and increase the temperature gradient [23]. There have been extensive theoretical and experimental studies of thermal counterflow [24–29]. In recent years, our lab has also conducted systematic characterization work on both steady-state [30–37] and transient counterflow [38–40] in bulk He II.

Nonetheless, when the heat transfer from a solid surface to the He II bath is concerned, the situation becomes complicated. There are two stable heat transfer regimes, i.e., the Kapitza regime at low heat fluxes and the film boiling regime at high heat fluxes [15,41]. In the Kapitza regime, the copper tube wall is in full contact with the He II, and the heat flux q_{He} depends on the temperatures T_w and T_{bath} through the following empirical correlation:

$$q_{He} = \alpha\left(T_w^n - T_{bath}^n\right), \tag{9}$$

where the parameters α and n strongly depend on the solid mate-rial and its surface quality [42–44]. Even for copper samples with apparently identical surface preparation, the Kapitza conductance can still vary by a factor of two. Noting the large uncertainties, we shall proceed with our analysis by adopting the measured values $\alpha = 0.5$ kW/m$^2 \cdot K^n$ and $n = 3.5$ for oxidized copper in He II [43].

As q_{He} reaches the peak heat flux q_0^*, a transition from the Kapitza regime to the film boiling regime occurs. During this tran-sient process, a vapor film develops and covers the copper sur-face, which leads to a rapid increase of the temperature difference $\Delta T = T_w - T_{bath}$. The value of q_0^* strongly depends on the heater geometry and the He II state, and it is characterized by the point where the He II adjacent to the interface exceeds the local boiling point. For a cylindrical heater of diameter D_2, q_0^* can be estimated as [15]:

$$q_0^*(T_{bath}, x) = \left(\frac{2\psi}{D_2/2}\int_{T_{bath}}^{T'(x)}\frac{dT}{f(T)}\right)^{1/3} \tag{10}$$

where $f(T) = A_{GM}\rho_n/(\rho_s s^4 T^3)$ is the He II heat conductivity func-tion, A_{GM} is the Gorter-Mellink mutual friction parameter [15], s is the He II specific entropy, ρ_n and ρ_s are the normal and the superfluid densities, respectively. The upper limit of the integral $T'(x) = min\{T_\lambda, T_{sat}(x)\}$, where $T_{sat}(x)$ is the saturation temperature at the local pressure, i.e., the sum of the vapor pressure at T_{bath} and the hydrostatic head pressure $P_h = \rho_{He}gh(x)$, where $h(x)$ is the He II depth at the location x along our tube. The empirical param-eter ψ, which depends on the heater radius, was originally intro-duced to account for the discrepancies between the ideal theory
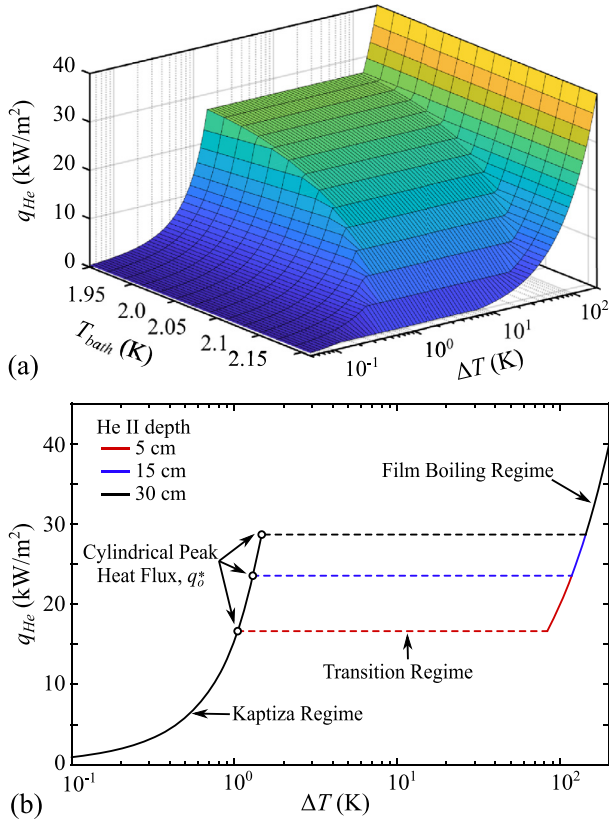
(a)

(b)

Fig. 4. (a) A representative graph of q_{He} as a function of T_{bath} and $\Delta T = T_w - T_{bath}$ with $\psi = 0.59$ and a He II depth of 15 cm. (b) Representative q_{He} curves at different He II depths with $\psi = 0.59$ and $T_{bath} = 2$ K.

Fig. 5. Simulated tube-wall temperature curves at the sensor locations with a tank pressure of 150 kPa. The optimal $\psi = 1.97$ is used in the model.

Table 1
Optimized ψ values in the peak heat flux model for He II runs at different tank pressures.

Tank Pressure (kPa)	Optimal ψ
50	0.43
100	0.59
150	1.97
200	1.96

(i.e., $\psi = 1$) and the measurement results [45,46]. Considering its possible dependance on the heat flux in transient heat transfer, we shall treat ψ as a tuning parameter in our model to best fit our observations.

In the film boiling regime, q_{He} can be estimated as [15]:

$$q_{\mathrm{He}} = h_{film}(T_w - T_{bath}), \qquad (11)$$

where the film boiling coefficient h_{film} is expected to depend on T_w, the tube radius, and the hydrostatic head pressure, but relevant experimental information is scarce. For cylindrical heaters with a surface temperature of about 40 K placed at a depth of 10 cm in He II, limited measurements suggest that h_{film} levels off at about 200 W/m^2·K when the diameter is greater than about 10 mm [15,47,48]. Since this depth is comparable to the average He II depth in our experiment and T_w is also similar, we shall adopt $h_{film} = 200$ W/m^2 · K in our simulations.

We must emphasize that the correlation model outlined above is devised for steady counterflow. A more realistic model for high-flux transient heat transfer from a cylindrical heater in He II should account for unique features in the buildup of the vortices and the emission of thermal waves [40], which is beyond the scope of the current work. On the other hand, following Ref. [15], we estimate that the heat diffusion time in He II at our observed heat fluxes is only a few milliseconds. Therefore, the quasi-steady correlation model should still yield useful information. Using the He II properties from the HEPAK$^{\mathrm{TM}}$ library [49], we can calculate q_{He} as a function of T_{bath} and ΔT. A representative graph is shown in Fig 4 (a) with $\psi = 0.59$ and a He II depth of 15 cm. In Fig 4 (b), we plot several q_{He} curves at different He II depths with $\psi = 0.59$ and $T_{bath} = 2$ K to show the depth effect. The different heat transfer regimes are also labeled for clarity.
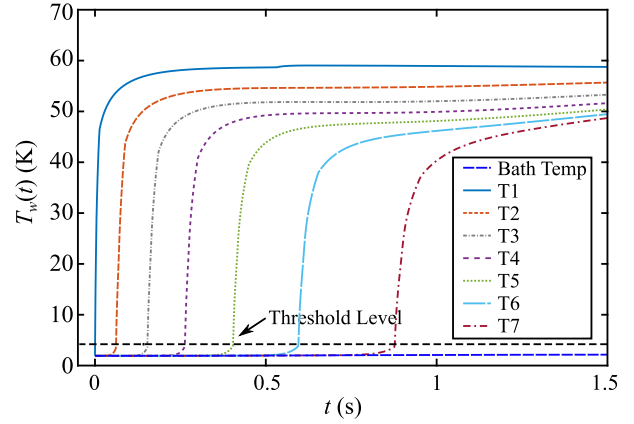
4. Model validation and fine-tuning

We have conducted numerical simulations using the governing equations as outlined in the previous section. These equations are solved using a two-step first-order Godunov-type finite-difference method [50,51] in the same computational domain as in our previous work [14]. Note that due to the finite volume of the He II in our experiment, the bath temperature T_{bath} was observed to rise by about 0.1-0.15 K in each run due to the heat deposition. Since the parameter q_0^* in our model depends on T_{bath}, we have implemented a time varying T_{bath} in our simulation using the experimental T_{bath} data.

In Fig. 5, we show the calculated tube-wall temperature curves at the sensor locations for a representative run with a tank pressure of 150 kPa. The empirical parameter $\psi = 1.97$ was used in this calculation. These temperature curves rise sharply to about 50 K upon the arrival of the gas front. The separation between adjacent temperature curves gradually increases, suggesting a slowing down of the propagation. These features all agree well with the experimental observations. These calculated temperature curves are also included in Fig. 2.

In Fig. 3, we include the calculated rise-time curves to compare with the experimental data obtained at various tank pressures. The profiles of these calculated curves depend on the choice of the ψ value. For each pressure, we tune ψ to minimize the total variance between the experimental rise times and the simulated rise times summed over all sensor locations. The ψ values obtained through this optimization procedure at different tank pressures are listed in Table 1. As one can see in Fig. 3, the optimized rise-time curves agree nicely with the experimental data in all the runs, which thereby confirms the fidelity of the model. This fine-tuned model with the optimal ψ will be used in our later calculation of the heat deposition in He II.

We would also like to briefly comment on the difference in the gas dynamics between our He I and He II experiments. Fig. 6 shows a comparison of He I and He II rise-time data obtained using the same upgraded tube system at a tank pressure of 150 kPa.
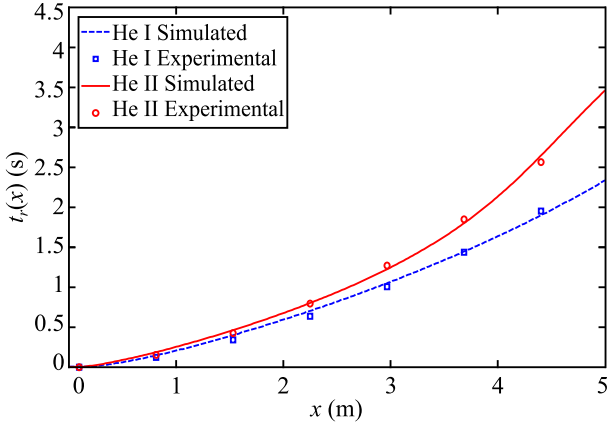
Fig. 6. Comparison of rise-time data in our He I and He II experiments using the same tube system with a tank pressure of 150 kPa.
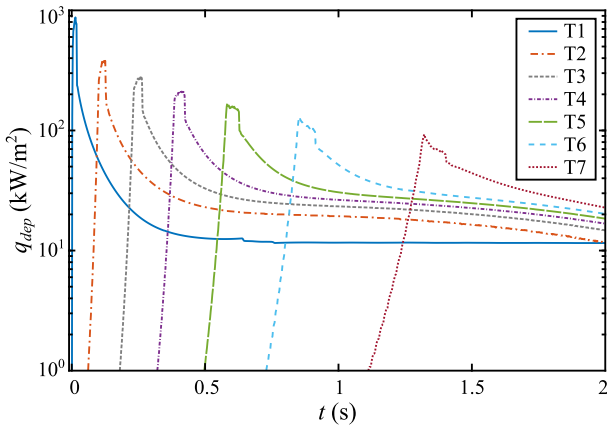

Fig. 7. Simulated heat flux q_{dep} deposited to the tube wall at the sensor locations for a representative run with a tank pressure of 100 kPa.

Fig. 8. Simulated heat flux into He II at the sensor locations for the runs with (a) 50 kPa tank pressure; and (b) 200 kPa tank pressure.

The optimal simulated curves are also included. It is clear that the He II curve shows a stronger slowing effect compared to the He I curve. This difference was suggested in early preliminary studies [52] but the result was compromised by various issues as discussed in Ref. [13]. Now we can draw a reliable conclusion that the He II cooled tube indeed has a stronger slowing effect on the gas propagation due to the more effective heat transfer in the bath.

5. Heat deposition in He II

We first calculate the total heat flux q_{dep} to the tube wall at the sensor locations using the optimized model. Fig. 7 shows the $q_{dep}(t)$ curves for a representative run with 100 kPa tank pressure. We see that all the q_{dep} curves first spike to above 10^2 kW/m². This spiking is associated with the arrival of the gas front, since the mass deposition rate $\dot{m}_c$ (and hence q_{dep}) is the highest when a clean and cold wall area is exposed to the gas. As the frost layer grows, the tube wall temperature T_w rises sharply to a saturation level of about 50 K (see Fig. 5), which leads to a rapid drop of $\dot{m}_c$ and q_{dep}. The nearly constant T_w in this saturation regime indicates a rough balance between q_{dep} and the heat flux q_{He} into the He II bath. At late times, the values of q_{dep} at the sensor locations are therefore controlled by the local $q_{He}(x)$.

Next, we evaluate the heat flux q_{He} to the He II bath. Fig. 8 (a) and (b) show the calculated q_{He} as a function of time at the sensor locations for the two runs with the lowest and the highest tank pressures (i.e., 50 kPa and 200 kPa), respectively. In both runs, q_{He} spikes up accompanying th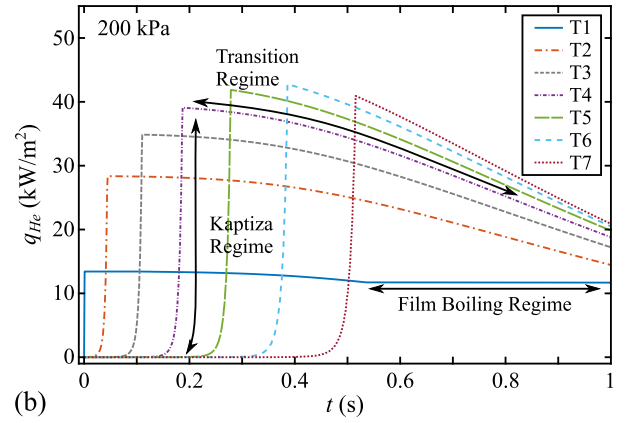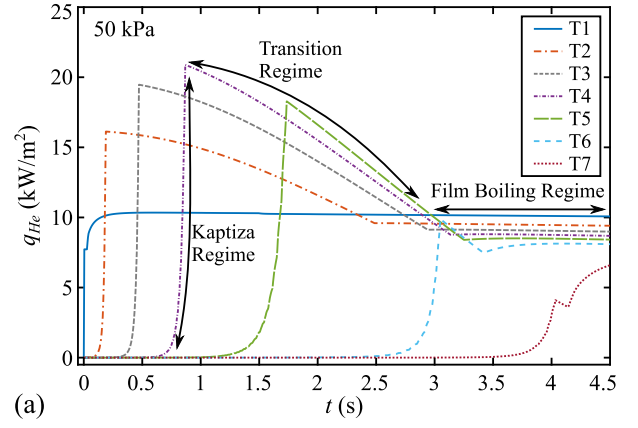e sharp rise of T_w, and the heat transfer in He II evolves promptly from the Kaptiza regime to the transition regime. In the transition regime, q_{He} is limited to the peak heat flux $q_0^*(T_{bath}, x)$, which is higher at a sensor location with a larger He II depth. Following the spike, q_{He} gradually drops, which is caused by the decrease in q_0^* as the bath temperature T_{bath} slowly increases (see Fig. 4 (a)). For the 50 kPa run, the q_{He} curves switch to a nearly constant level at most of the sensor locations after about 3 s. This leveling-off is caused by film boiling, since q_{He} in this regime is dominantly controlled by the saturated tube-wall temperature T_w. In the higher pressure runs, the time takes for the gas to reach the tube end can be shorter than the transition time from the Kaptiza regime to the film boiling regime in He II. As a consequence, the leveling-off film boiling regime may not show up in the q_{He} curves in these runs.

We have also calculated the total heat deposited in the bath from the entire tube as a function of time:

$$Q(t) = \int_0^t dt' \int_0^L dx' \pi D_2 \cdot q_{He}(x', t'). \tag{12}$$

The results for all the four runs are collected in Fig. 9. We terminate the $Q(t)$ curves at the time when the gas front reaches the location of the last sensor. It appears that after a short transient, $Q(t)$ increases roughly linearly with time for all the runs. The rate of the total heat deposition dQ/dt in this linear regime increases with increasing the tank pressure. By the time the last sensor temperature spikes, about 12 kJ is deposited in the He II bath in the 50 kPa run, whereas less than 5 kJ is deposited in the 200 kPa run due to the much shorter gas propagation time.
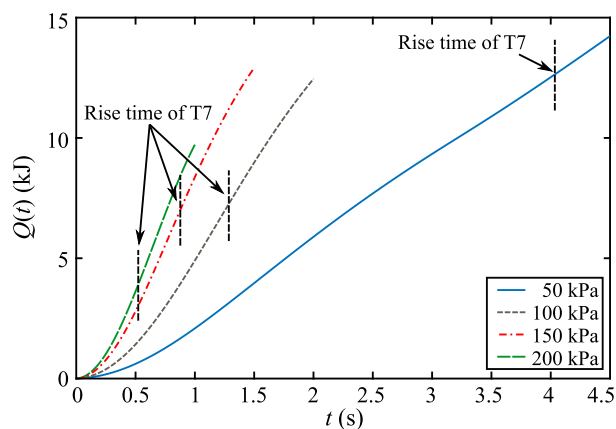
Fig. 9. Calculated total heat $Q(t)$ deposited in the He II bath under different tank pressures. The vertical dashed line marks the time when the gas front reaches the last sensor.

6. Summary

We have conducted systematic experimental and numerical studies of N_2 gas propagation and condensation inside an evacuated copper tube cooled by He II. By adjusting the tuning parameter ψ in our He II heat transfer model, we are able to reproduce the observed tube-wall temperature variations in all the runs with different tank pressures. The fine-tuned model is then used to calculate the heat flux to the He II bath. Our results reveal that upon the arrival of the gas front, the heat flux to He II spikes up to the peak heat flux which then gradually drops with time due to the rise of the bath temperature. In the run where the transition to the film boiling regime completes before the gas front reaches the tube end, we observe that the heat flux to the bath levels off as controlled by the film boiling. We have also evaluated the total heat deposited in the bath and found that the rate of the total heat deposition increases with increasing the tank pressure. The knowledge produced in this study may benefit the design of future beamline systems cooled by He II.

We would also like to point out that in our study we observed a more or less constant mass deposition rate in the tube section where the gas front has passed. A similar phenomenon was seen in our previous He I work as well [14]. These observations suggest that in a sufficiently long tube such as an accelerator beamline tube, the gas flushing into the tube would eventually be almost consumed by the mass deposition on the tube inner wall after a certain propagation range. This maximum range of frost contamination is a useful parameter in beamline research and design. We plan to explain the physical mechanism underlying this nearly constant mass deposition rate and present a simple correlation that allows reliable evaluation of the maximum contamination range in a future publication.

Declaration of Competing Interest

The undersigned hereby declare that the manuscript is original, does not infringe any copyright or other proprietary rights of third parties, is not submitted for publication to another journal, and has not been previously published.

Acknowledgments

The authors would like to thank Prof. S. W. Van Sciver for valuable discussions. This research is supported by the U.S. Department of Energy under Grant No. DE-SC0020113 and was conducted at the National High Magnetic Field Laboratory at Florida State University, which is supported through the National Science Foundation Cooperative Agreement No. DMR-1644779 and the state of Florida.

References

[1] P. Lebrun, L. Tavian, Cooling with Superfluid Helium, Tech. Rep. ArXiv:1501.071562014, CERN, 10.5170/CERN-2014-005.453.
[2] C. Pagani, P. Pierini, Cryomodule design, assembly and alignment, in: Proc. of 12th Int. Work. on RF Supercond., Ithaca NY, 2005. Accessed: 2021-04-27.
[3] M. Wiseman, K. Crawford, M. Drury, K. Jordan, J. Preble, Q. Saulter, W. Schneider, Loss of cavity vacuum experiment at CEBAF, in: P. Kittel (Ed.), Adv. in Cryog. Eng., Adv. in Cryog. Eng., volume 39, Springer US, Boston, MA, 1994, pp. 997–1003, doi:10.1007/978-1-4615-2522-6_121.
[4] M. Seidel, D. Trines, K. Zapfe, Failure Analysis of the Beam Vacuum in the Superconducting Cavities of the TESLA Main Linear Accelerator, Tech. Rep. TESLA-Report 2002-06, DESY, 2002.
[5] M. Ady, M. Hermann, R. Kersevan, G. Vandoni, D. Ziemianski, Leak propagation dynamics for the HIE-ISOLDE superconducting linac, in: Proc. of the 5th Int. Particle Accelerator Conf., Dresden, Germany, 2014, pp. 2351–2353, doi:10.18429/jacow-ipac2014-wepme039.
[6] M. Ady, G. Vandoni, M. Guinchard, P. Grosclaude, R. Kersevan, R. Levallois, M. Faye, Measurement Campaign of 21–25 July 2014 for Evaluation of HIE-ISOLDE Inrush Protection System, Tech. Rep. EDMS No. 1414574, CERN, 2014.
[7] T. Boeckmann, D. Hoppe, K. Jensch, R. Lange, W. Maschmann, B. Petersen, T. Schnautz, Experimental tests of fault conditions during the cryogenic operation of a XFEL prototype cryomodule, in: Proc. of the Int. Cryog. Eng. Conf. 22 - Int. Cryog. Mater. Conf., Seoul, Korea, 2008, p. 723728.
[8] A.A. Dalesandro, J. Theilacker, S.W. Van Sciver, Experiment for transient effects of sudden catastrophic loss of vacuum on a scaled superconducting radio frequency cryomodule, in: AIP Conf. Proc., vol. 1434, Spokane, Washington, USA, 2012, pp. 1567–1574.
[9] R. Dhuley, S.W. Van Sciver, Propagation of nitrogen gas in a liquid helium cooled vacuum tube following sudden vacuum loss Part I: experimental investigations and analytical modeling, Int. Heat Mass Transf. 96 (2016) 573–581, doi:10.1016/j.ijheatmasstransfer.2016.01.077.
[10] R.C. Dhuley, S.W. Van Sciver, Propagation of nitrogen gas in a liquid helium cooled vacuum tube following sudden vacuum loss Part II: analysis of the propagation speed, Int. Heat Mass Transf. 98 (2016) 728–737, doi:10.1016/j.ijheatmasstransfer.2016.03.077.
[11] N. Garceau, W. Guo, T. Dodamead, Gas propagation following a sudden loss of vacuum in a pipe cooled by He I and He II, IOP Conf. Ser.: Mater. Sci. Eng. 278 (2017) 012068, doi:10.1088/1757-899x/278/1/012068.
[12] N. Garceau, S. Bao, W. Guo, S.W. Van Sciver, The design and testing of a liquid helium cooled tube system for simulating sudden vacuum loss in particle accelerators, Cryogenics 100 (2019) 92–96, doi:10.1016/j.cryogenics.2019.04.012.
[13] N. Garceau, S. Bao, W. Guo, Heat and mass transfer during a sudden loss of vacuum in a liquid helium cooled tube Part I: interpretation of experimental observations, Int. Heat Mass Transf. 129 (2019) 1144–1150, doi:10.1016/j.ijheatmasstransfer.2018.10.053.
[14] N. Garceau, S. Bao, W. Guo, Heat and mass transfer during a sudden loss of vacuum in liquid helium cooled tube - Part II: theoretical modeling, Int. J. Heat Mass Transf. 146 (2020), doi:10.1016/j.ijheatmasstransfer.2019.118883.
[15] S.W. Van Sciver, Helium Cryogenics, International Cryogenics Monograph Series, 2nd ed., Springer, New York, 2012. ISBN 978-1-4419-9978-8 978-1-4419-9979-5.
[16] N. Garceau, S. Bao, W. Guo, Effect of mass flow rate on gas propagation after vacuum break in a liquid helium cooled tube, IOP Conf. Ser.: Mater. Sci. Eng. 755 (2020) 012112, doi:10.1088/1757-899x/755/1/012112.
[17] R. Dhuley, S.W. Van Sciver, Epoxy encapsulation of Cernox™ SD thermometer for measuring the temperature of surfaces in liquid helium, Cryogenics 77 (2016) 49–52, doi:10.1016/j.cryogenics.2016.05.001.
[18] C. Weber, A. Henriques, S. Grohmann, Study on the heat transfer of helium cryostats following loss of insulating vacuum, IOP Conf. Ser.: Mater. Sci. Eng. 502 (2019) 012170, doi:10.1088/1757-899x/502/1/012170.
[19] A. Kopczynski, B. Baran, Z. Malecha, Numerical study of a consequence of a vacuum insulation degradation in a cryogenic system, IOP Conf. Ser.: Mater. Sci. Eng. 755 (2020) 012115, doi:10.1088/1757-899x/755/1/012115.
[20] J. Collier, J. Thome, Convective Boiling and Condensation, 3rd ed., Oxford University Press, New York, 1994. ISBN 0-19-85628-9.
[21] A.H. Persad, C.A. Ward, Expressions for the evaporation and condensation coefficients in the Hertz-Knudsen relation, Chem. Rev. 116 (14) (2016) 7727–7767, doi:10.1021/acs.chemrev.5b00511.
[22] D.R. Tilley, J. Tilley, Superfluidity and Superconductivity, Graduate Student Series in Physics, 2nd ed., Adam Hilger Ltd, Bristol, 1986. ISBN 9780852748077.
[23] W.F. Vinen, Mutual friction in a heat current in liquid helium II III. Theory of the mutual friction, Proc. R. Soc. Lond. A 242 (1231) (1957) 493–515, doi:10.1098/rspa.1957.0191.
[24] K.W. Schwarz, Turbulence in superfluid helium: steady homogeneous counterflow, Phys. Rev. B 18 (1978) 245–262, doi:10.1103/PhysRevB.18.245.
[25] K.P. Martin, J.T. Tough, Evolution of superfluid turbulence in thermal counterflow, Phys. Rev. B 27 (1983) 2788–2799, doi:10.1103/PhysRevB.27.2788.

[26] G.P. Bewley, M.S. Paoletti, K.R. Sreenivasan, D.P. Lathrop, Characterization of re-connecting vortices in superfluid helium, Proc. Natl. Acad. Sci. U.S.A. 105 (37) (2008) 13707–13710, doi:10.1073/pnas.0806002105.

[27] T.V. Chagovets, S.W. Van Sciver, A study of thermal counterflow using particle tracking velocimetry, Phys. Fluids 23 (10) (2011) 107102, doi:10.1063/1.3657084.

[28] Y. Mineda, M. Tsubota, Y.A. Sergeev, C.F. Barenghi, W.F. Vinen, Velocity distributions of tracer particles in thermal counterflow in superfluid ^{4}He, Phys. Rev. B 87 (2013) 174508, doi:10.1103/PhysRevB.87.174508.

[29] P. Švančara, P. Hrubcová, M. Rotter, M. La Mantia, Visualization study of thermal counterflow of superfluid helium in the proximity of the heat source by using solid deuterium hydride particles, Phys. Rev. Fluids 3 (2018) 114701, doi:10.1103/PhysRevFluids.3.114701.

[30] A. Marakov, J. Gao, W. Guo, S.W. Van Sciver, G.G. Ihas, D.N. McKinsey, W.F. Vinen, Visualization of the normal-fluid turbulence in counterflowing superfluid ^{4}He, Phys. Rev. B 91 (9) (2015) 094503, doi:10.1103/PhysRevB.91.094503.

[31] J. Gao, W. Guo, V.S. L'vov, A. Pomyalov, L. Skrbek, E. Varga, W.F. Vinen, Decay of counterflow turbulence in superfluid ^{4}He, JETP Lett. 103 (10) (2016) 648–652, doi:10.1134/S0021364016100064.

[32] J. Gao, E. Varga, W. Guo, W.F. Vinen, Energy spectrum of thermal counterflow turbulence in superfluid helium-4, Phys. Rev. B 96 (2017) 094511, doi:10.1103/PhysRevB.96.094511.

[33] J. Gao, E. Varga, W. Guo, W.F. Vinen, Statistical measurement of counterflow turbulence in superfluid helium-4 using He$_2^*$ tracer-line tracking technique, J. Low Temp. Phys. 187 (2017) 490, doi:10.1007/s10909-016-1681-y.

[34] S. Bao, W. Guo, V.S. L'vov, A. Pomyalov, Statistics of turbulence and intermittency enhancement in superfluid ^{4}He counterflow, Phys. Rev. B 98 (2018) 174509, doi:10.1103/PhysRevB.98.174509.

[35] B. Mastracci, W. Guo, Exploration of thermal counterflow in He II using particle tracking velocimetry, Phys. Rev. Fluids 3 (6) (2018) 063304, doi:10.1103/PhysRevFluids.3.063304.

[36] B. Mastracci, W. Guo, Characterizing vortex tangle properties in steady-state He II counterflow using particle tracking velocimetry, Phys. Rev. Fluids 4 (2) (2019) 023301, doi:10.1103/PhysRevFluids.4.023301.

[37] B. Mastracci, S. Bao, W. Guo, W.F. Vinen, Particle tracking velocimetry applied to thermal counterflow in superfluid ^{4}He: motion of the normal fluid at small heat fluxes, Phys. Rev. Fluids 4 (2019) 083305, doi:10.1103/PhysRevFluids.4.083305.

[38] S. Bao, W. Guo, Quench-spot detection for superconducting accelerator cavities via flow visualization in superfluid helium-4, Phys. Rev. Appl. 11 (4) (2019) 044003, doi:10.1103/PhysRevApplied.11.044003.

[39] S. Bao, T. Kanai, Y. Zhang, L.N. Cattafesta, W. Guo, Stereoscopic detection of hot spots in superfluid ^{4}He (He II) for accelerator-cavity diagnosis, Int. J. Heat Mass Transf. 161 (2020) 120259, doi:10.1016/j.ijheatmasstransfer.2020.120259.

[40] S. Bao, W. Guo, Transient heat transfer of superfluid ^{4}He in nonhomogeneous geometries: second sound, rarefaction, and thermal layer, Phys. Rev. B 103 (2021) 134510, doi:10.1103/PhysRevB.103.134510.

[41] M. Murakami, S. Takada, M. Nozawa, Study of He II boiling flow field around a heater, IOP Conf. Ser.: Mater. Sci. Eng. 101 (2015) 012165, doi:10.1088/1757-899x/101/1/012165.

[42] G. Claudet, P. Seyfert, Bath cooling with subcooled superfluid helium, Adv. Cryog. Eng. 27 (1981) 441.

[43] A. Kashani, S.W. Van Sciver, High heat flux Kapitza conductance of technical copper with several different surface preparations, Cryogenics 25 (5) (1985) 238–242, doi:10.1016/0011-2275(85)90202-4.

[44] A. Iwamoto, R. Maekawa, T. Mito, Kapitza conductance of an oxidized copper surface in saturated He II, Cryogenics 41 (5) (2001) 367–371, doi:10.1016/S0011-2275(01)00082-0.

[45] S.W. Van Sciver, R. Lee, Heat transfer to helium-II in cylindrical geometries, in: Adv. Cryog. Eng., vol. 35, Springer US, Boston, MA, 1980, pp. 363–371.

[46] S.W. Van Sciver, R. Lee, Heat transfer from circular cylinders in He II, in: Cryogenic Process and Equipment in Energy Systems, vol. H00164, ASME Publication, Boston, MA., 1981, p. 147.

[47] J.S. Goodling, R.K. Irey, Non-boiling and film boiling heat transfer to a saturated bath of liquid helium, in: Adv. Cryog. Eng., vol. 14, Springer US, Boston, MA, 1969, pp. 159–169.

[48] K. Bretts, A. Leonard, Free convection film boiling from a flat, horizontal surface in saturated He II, in: Adv. in Cryog. Eng., vol. 21, Springer US, Boston, MA., 1975, pp. 282–292. 10.1007/978-1-4757-0208-8_37

[49] V. Arp, B. McCarty, J. Fox, HEPAK, (Cryodata Inc.), 2005.

[50] I. Danaila, P. Joly, S. Kaber, M. Postel, An Introduction to Scientific Computing: Twelve Computational Projects Solved with MATLAB, Springer-Verlag, New York, 2007, doi:10.1007/978-0-387-49159-2.

[51] G. Sod, A survey of several finite difference methods for systems of nonlinear hyperbolic conservation laws, J. Comput. Phy. 27 (1) (1978) 1–31, doi:10.1016/0021-9991(78)90023-2.

[52] R.C. Dhuley, Gas propagation in a liquid helium cooled vacuum tube following a sudden vacuum loss, Florida State University, Tallahassee, 2016 Dissertation. Retrieved from FSU, Proquest Diss. Publishing database (UMI No. 10120583)